

THE PECULIAR INFRA-RED EMISSION OF SN 2014DT

Master Thesis

CAMILLE LANDRI



UPPSALA
UNIVERSITET

Department of Physics and Astronomy

Supervisor: Dr. Joel Johansson

September 2019

Abstract

This work intends to analyse the late time photometry of the Type Iax Supernova (SN) 2014dt, and test different models against the observations. The optical and near-IR photometry of the SN are presented, as well as the late time (300 to 800 days post-maximum) mid-IR observations made with the Spitzer 3.6 and 4.5 μm channels, in which a strong excess of emission is detected. This excess also affects the bolometric luminosities and spectral energy distributions (SEDs) of SN 2014dt, which show strong divergences from other Iax SNe 2005hk and 2012Z. The bolometric light curve (LC) is then modelled using the radioactive decays occurring in the ejecta. The early LC (up to 300 days) is successfully described by a dense, optically thick inner component and a lighter, optically thin outer component. This model is tested against late time luminosities, and while it fails to describe the excess itself, it tends to match the rest of the LC. The effects of warm dust surrounding the SN are examined, as well as a corresponding model, which is used along with a BB to explain the two-peak shape observed in the SED during the epoch of excess. The observations are consistent with $10^{-5} M_{\odot}$ of 0.1 μm graphitic dust at 700 K, and the late phase near-IR spectra of the SN shows potential CO emission lines, which could confirm the dust hypothesis. Possible heating scenarios for pre-existing dust are then discussed, radiative heating is unlikely to be efficient enough but requires more testing to be fully ruled out, while shock heating needs further constraining.

Popular Introduction in Swedish

När stjärnor närmar sig sin sista livsfas kan deras inre balans lätt störas. När en vit dvärgstjärna når en kritisk massa, genom någon slags massöverföring från en grannstjärna, utlöses en explosion. Denna explosion leder till en Typ Ia supernova, och eftersom den kritiska massan är universell för dessa supernovor har de nästan identisk ljusstyrka vid sitt intensitetsmaximum - en kvalitet som gör dem mycket användbara som avståndsindikatorer inom astronomin.

En viss kategori av dessa "vit-dvärg-explosioner" verkar dock skilja sig mycket från normala Typ Ia supernovor, på grund av olika explosionsförhållanden och mekanismer som är långt ifrån förstådda. Detta arbete fokuserar på en av dessa egendomliga supernovor: Typ Iax SN 2014dt, som vid sena tidpunkter visade en stark emission av infrarött ljus (vid våglängder på 1-5 mikrometer).

Först analyserar vi optisk och infraröd fotometri och studerar hur den spektrala energifördelningen förändras över tid. Sedan övervägs två möjliga källor för den infraröda emissionen; som kan komma från olika radioaktiva sönderfall i supernovan och en eventuell reststjärna, eller från ett upphettat stoftmoln som omger supernovan.

Det första förslaget verkar inte förklara detta överskott, medan modeller med termisk emission från upphettat stoft kring supernovan är förenligt med observationerna. Hypotesen med radioaktivt sönderfall från två olika komponenter kräver en mer avancerad analys, eftersom endast enkla modeller har beaktats i detta arbete. Å andra sidan kräver närvaron av ett stoftskal ytterligare studier, då upphettningsmekanismen är okänd.

Table of Contents

Abstract	II
Popular Introduction in Swedish	II
List of Figures	V
List of Tables	VI
1 Introduction	1
1.1 The Type Ia group	1
1.1.1 Progenitors	1
1.1.2 Explosion Mechanism	2
1.1.3 Standardisation	2
1.1.4 Subgroups	2
1.2 Type Iax Supernovae	3
1.2.1 General Properties	3
1.2.2 Explosion Mechanism	4
1.3 SN 2014dt	5
1.3.1 Current Results	5
1.3.2 Distance derivation	6
1.3.3 Peak Epoch	6
1.3.4 Other SNe used in this work	7
2 The Photometry of SN 2014dt	8
2.1 Observations	8
2.1.1 Results	8
2.1.2 Analysis	10
2.2 Bolometric Light Curve	10
2.2.1 Results	11
2.2.2 Analysis and Discussion	11
2.3 Spectral Energy Distribution	13
2.3.1 Overall Evolution	13
2.3.2 SEDs at the Epochs of IR Excess	13
3 The Two Component Light Curve Model	17
3.1 Radioactive Decay and Decline Rate	17
3.2 Describing the LC With Two Components	18

3.3	Modelling the Late-Time Optical Output	19
3.3.1	Results	19
3.3.2	Discussion	20
4	Warm Dust	22
4.1	Dust Model	22
4.1.1	Results	23
4.1.2	Discussing the Spectroscopy	25
4.2	Heating Mechanism	27
4.2.1	Radiative Heating	27
4.2.2	Shock Heating	28
5	Conclusion	30
	Literature	32
A	Decline Rates	35

List of Figures

Figure 1.1: Phillips Relation for Type IA and Iax SNe	3
Figure 1.2: Spectral comparison of Type Ia 2011fe and Type Iax 2005hk at early phases.	4
Figure 1.3: Comparison of SNe 2014dt and 2005hk spectra at early phases	6
Figure 2.1: Multi-band light curves of SN 2014dt	9
Figure 2.2: Bolometric light curve of SN 2014dt	12
Figure 2.3: Bolometric light curve of SNe 2014dt, 2012Z and 2005hk	12
Figure 2.4: Evolution of the SED of SN 2014dt	15
Figure 2.5: SEDs at 300, 500 and 700 days	16
Figure 3.1: Optical Bolometric light curve of SN 2014dt from Kawabata et al. (2018)	18
Figure 3.2: Optical, near and mid-IR Bolometric light curve of SN 2014dt against the two components LC model	19
Figure 4.1: Comparison of 2014dt absolute magnitude obtained with Spitzer $4.5\mu m$ channel to other Ia and Ia-CSM SNe.	22
Figure 4.2: Evolution of the emission efficiency factor depending on the grain radius	23
Figure 4.3: Fit of the SED at 300, 500 and 700 days wit a BB component and a warm dust component	24
Figure 4.4: Fit of the SED at 550 days with a BB component and a warm dust component with spectroscopy on top	26
Figure 4.5: Spectroscopy of SN 2014dt at 542 days between 2 and $2.4\mu m$	26
Figure 4.6: Dust masses obtained from fitting the SEDs at different epochs	28
Figure 4.7: Post-shock dust temperature as a function of post-shock electron temperature and density	29

List of Tables

Table 2.1: BB Fit Parameters obtained in figure 2.3.1	14
Table 3.1: Two Component LC parameters obtained in figure 3.1 against the range suggested by Kawabata et al. (2018).	19
Table 3.2: Two Component LC parameters obtained in figure 3.2 against the range suggested by Kawabata et al. (2018).	20
Table 4.1: Black body and dust fit Parameters	25
Table A.1: Absolute magnitude decline rates for each filters	35
Table A.2: Bolometric luminosity decline rates ($\log(\text{erg.s}^{-1}).\text{day}^{-1}$)	35

1 Introduction

Nothing quite compares to the death of a star. The explosion it triggers, called Supernova, is very common and is thought to occur in two distinct scenarios. When a star heavier than $8M_{\odot}$ runs out of fuel for nuclear reactions, its own gravitational forces are not counteracted anymore and the star collapses. This core-collapse (CC) induces an explosion, which can have different consequences that depend strongly on the nature of the star, for example some lead to the formation of Black Holes while others do not leave a remnant behind. On the other hand, a supernova can also occur in some types of binary systems, consisting of a White Dwarf (WD) accreting material from a companion star. The WD then undergoes a thermal explosion once enough material has been gathered to threaten its internal balance. Although these two scenarios could describe a possible taxonomy for the SNe, they are actually categorized by spectroscopic and photometric features. A SN showing Hydrogen lines in its spectra belongs to the Type II group, while the absence of such lines assigns it to the Type I group. Each class is then further divided into sub-classes, defined by some peculiarities found in the observations. The CC mechanism seems to occur for every subgroup but one, the Type Ia, which is thought to be caused by thermal explosions. Not all the conditions giving rise to Ia SNe are well constrained, but the study of these objects yielded some considerable insights about the universe, which greatly increased their renown among astronomers.

1.1 The Type Ia group

Type Ia SNe are very important objects in astrophysics and cosmology. With a peak absolute magnitude around -19.5 in the B-band, they are some of the brightest SNe one can observe. Their spectra are characterized by strong silicon absorption lines at early times, and show ejecta speed of the order of $10\,000\text{ km/s}$. They do not seem to favour any type of galaxy but are expected to occur in old systems since they involve White Dwarfs, the last life stage of certain stars.

1.1.1 Progenitors

The nature of their progenitor systems is not well understood, but evidence point towards a binary system composed of a Carbon/Oxygen White Dwarf (CO WD) accreting matter from a companion star. While few doubts subsist about the former component, the characteristics of the companion star remain unclear. Most observations are consistent with a Helium star, but also tend to agree with other types of star. Thus, the

companion could consist of a Hydrogen-rich star, it could be a giant or belong to the main-sequence or even be another WD. The progenitor systems are then classified into two types: the single-degenerate (SD) systems, consisting of a WD and a non-degenerate companion; and the double-degenerate (DB) systems, with two WD.

1.1.2 Explosion Mechanism

When enough material has been gathered to get close to the Chandrasekhar Mass ($M_{Ch} \sim 1.4M_{\odot}$), under which the electron degeneracy cannot withstand the gravitational forces anymore, the increasing pressure inside the WD ignites carbon burning. The energy released by the carbon fusion causes disturbances that will eventually trigger a subsonic combustion, called deflagration, which then transitions to a supersonic combustion, called detonation. The nuclear burning allows for the production of heavier elements like iron and nickel. This nucleosynthesis not only explains how iron is continually produced and ejected in the universe, it is also responsible for the brightness of the SN.

1.1.3 Standardisation

The optical output of the SNe is caused by the radioactive decay of ^{56}Ni , and since the WDs explode around M_{Ch} , the mass of ^{56}Ni synthesized during the explosion does not differ much from one event to another. This means the LCs of Type Ia all have a similar shape, and one can empirically relate the optical peak of a SN, caused by the quantity of nickel formed during the explosion, to its early optical output decline rate, induced by the decays of ^{56}Ni (see fig. 1.1). This relation, called the "Phillips Relation" (Phillips et al., 1999), is very important for astronomers because it allows for LC standardisation, meaning that Type Ia SNe can actually be used as Standard(-isable) Candles. This feature also provided the first observational evidence for the accelerating expansion of the Universe, since Type Ia SNe were the first object whose distance was derived at high precision.

1.1.4 Subgroups

Overall, the Type Ia is thought to be a very homogeneous group of SNe, with very few divergences from the standard templates. However, there are some outliers among these objects, showing great differences from one or several standard features. These anomalies are actually frequent enough to give rise to subgroups of Type Ia SNe. Naturally, these curiosities share a common characteristic: they do not obey the Phillips Relation. Then, one can regroup them depending on some peculiar spectroscopic or photometric feature. There exist many sub-classes, all defined by the shape of their LC, their peak brightness and their spectroscopy. While the mechanisms responsible for these peculiarities are still unclear, they are likely to be explained by different progenitors and explosion scenarios. Some divergences from the standard Ia are more notable than others, for

example, Super-Chandrasekhar SNe seem to explode with a mass significantly greater than M_{Ch} , which implies fairly unusual mass conditions that is likely to be achieved by the merging of two WD. Some other SNe appear to strongly interact with their Hydrogen-rich Circumstellar Medium (CSM), giving rise to a subgroup called Ia-CSM (Silverman et al., 2013), such behaviour was only observed among Type IIn SNe and could indicate a different explosion mechanism. Among all these sub-classes, one is of particular interest in this work, the so-called Type Iax Supernovae.

1.2 Type Iax Supernovae

In 2002, a SN with curious characteristics was discovered, SN 2002cx (Li et al., 2003). Indeed, its overall features could easily be related to the Type Ia, but also differed from these SNe on several important points. Its brightness rise and decline rates, as well as some spectral lines, did not match any other Ia SN, and it does not follow the Phillips Relation (see fig. 1.1). Further discoveries of similar objects led to the reclassification of Ia SNe to include these objects under the category "Peculiar Type Ia" or "2002cx-like" SNe, later renamed by Foley et al. (2013) as Type Iax SNe.

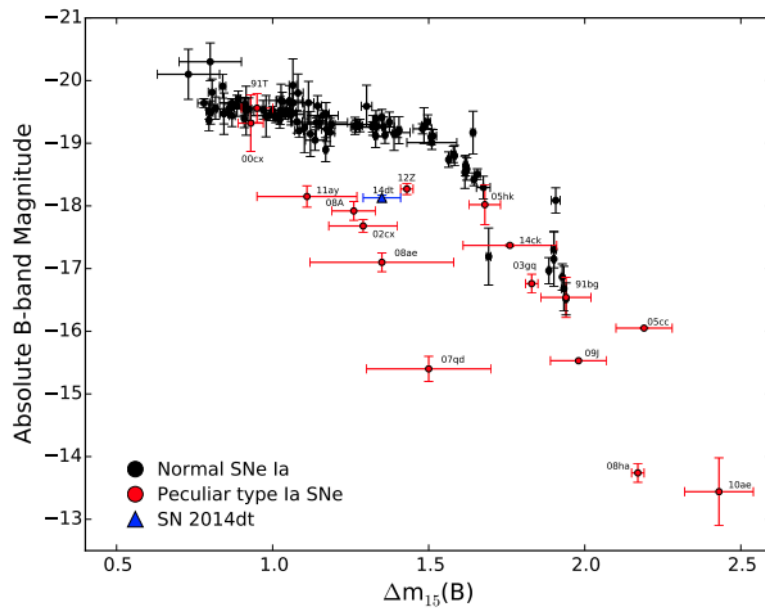


Figure 1.1: Relation between absolute B-band maximum and δm_{15} (Phillips Relation) for Type Ia and Iax SNe.

1.2.1 General Properties

These SNe are regrouped according to several particular features. The shape of their LCs is similar to a Normal Ia, but are actually less luminous by at least 1 mag and the brightness rises faster in every band. Furthermore, while the decline rates in the B-V bands are slightly steeper, they are significantly slower in the redder bands, and the

SNe do not show much colour evolution. Concerning their spectra, they match the spectral evolution of Ia SNe at early times (see figure 1.2), but differ greatly in their late phase. Any SN goes through a nebular phase at late times: their spectra are dominated by forbidden lines and one can actually observe the expanding ejecta as they become optically thin. Iax SNe, on the other hand, do not seem to become fully nebular, as their spectra still shows permitted lines in the late phase. Their ejecta speed is also slower: the expansion velocities measured using Si II lines range between 7 000 and 2 000 km/s compared to 10 000 km/s for a typical Ia.

Moreover, Iax SNe distribution seems to favour star-forming late-type host galaxies, and the similarities between Type Ia and Iax could indicate similar progenitors, a binary system with a CO WD. Since Iax SNe seem to occur in young star populations, the binary system should produce and explode star quickly. Assuming that the explosion occurs at Chandrasekhar Mass, the quickest way to get a CO WD to explode is through He accretion from a He star companion. Although this possibility is far from being confirmed, McCully et al. (2014) found a bright and blue system at the location of a well-studied Type Iax, SN 2012Z, before the explosion, which is likely to be its progenitor. They further argued that it could be a He star companion, which is consistent with the hypothesis made above.

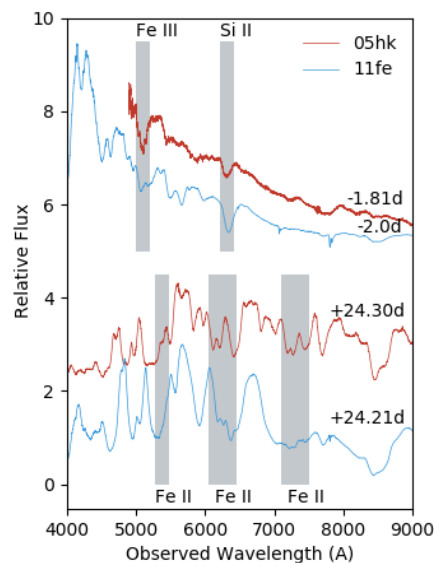


Figure 1.2: Comparison of Type Ia 2011fe and Type Iax 2005hk spectra at 2 days before and 24 days after brightness peak. The strong Fe II, Fe III and Si II features are denoted in grey. Data from Phillips et al. (2007) for 2005hk and Parrent et al. (2012), Pereira et al. (2013) for 2011fe.

1.2.2 Explosion Mechanism

Amongst all the properties of Type Iax SNe, the least understood is their explosion mechanism. A wide range of models have been proposed, some even diverge completely from the Normal Ia SNe explosions and include core-collapse, though a large

quantity of evidence (Jha, 2017) points towards the thermonuclear explosion of a WD. However, instead of transitioning from a deflagration to a detonation like Type Ia do, the combustion would stay subsonic. The combination of low values but large variations of kinetic energies in the ejecta is consistent with a subsonic deflagration, which would result in a well-mixed ejecta, while a detonation would give rise to a layered structure. Furthermore, the late time velocities are below the escape velocities of the WD, which means the explosion would not release enough energy to unbind the star entirely, leaving behind a bound remnant. This could explain why Iax SNe don't become fully nebular at late times, and would also result in an optically thick wind driven by the radioactive decays occurring in the bound remnant. Although this model, called Pure Deflagration (PD), shows great promises, there is still a tremendous amount of work left to characterize the explosions of Iax SNe.

1.3 SN 2014dt

SN 2014dt was discovered post-maximum in the galaxy Messier 61 on 2014 October 29.838 UT (JD = 2456960.338) by Nakano et al. (2014), with an apparent magnitude of 13.6 in the V band. It was shortly classified as a Type Iax SN thanks to spectroscopic observations made on October 31.2 UT with the 182 cm Copernico Telescope (Ochner et al., 2014).

1.3.1 Current Results

The early observations of SN 2014dt are fairly regular, its early spectra are similar to other Iax SNe, featuring numerous Fe II lines around 5 200, 6 100 and 7 200 Å (see 1.3). Early time LCs showed some of the slowest declines observed in Type Ia and Iax, and apart from a noticeably low luminosity, did not diverge much from the LCs of its peers. Several models were proposed to explain the shape of the LC, and the most successful one (up to 300 days post maximum) describes ejecta consisting of two layers with different density and optical depth (Kawabata et al., 2018). Foley et al. (2015) constrained the progenitor system to a CO WD accreting from a He Star. However, after 250 days the SN starts to exhibit an excess of emission in the mid-IR channels, which has never been witnessed for Type Iax SNe. Although no evidence for dust formation was found (Foley et al., 2016), Fox et al. (2016) argue in favour of warm dust, either pre-existing or newly formed. Other sources of such emission could be the wind caused by a bound remnant or the fallback it induces when accreting surrounding material.

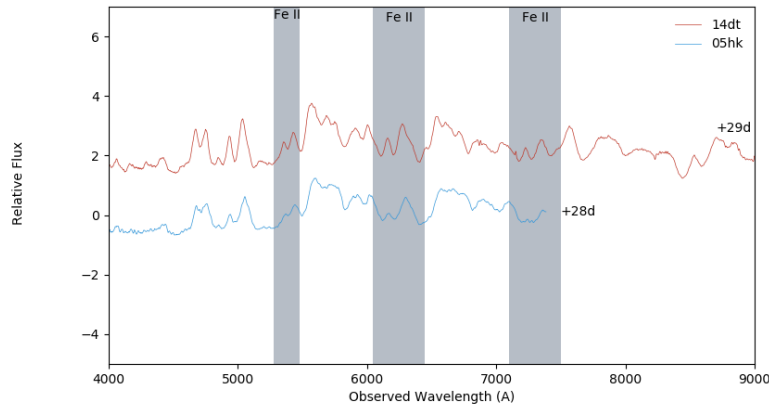


Figure 1.3: Comparison of SNe 2014dt and 2005hk spectra at 29-475 and 28-463 days respectively after brightness peak. The most noticeable Fe II features are added in grey. Data from Foley et al. (2015) for 2014dt and Blondin et al. (2012) for 2005hk

1.3.2 Distance derivation

SN 2014dt is located in Messier 61 which is a relatively close galaxy. Recent distance measurements of this galaxy range between 12.2 Mpc (Roy et al., 2011) and 20.7 Mpc (Rodríguez et al., 2014) depending on the method used. Some studies of SN 2014dt (Foley et al., 2015) prefer to use the smaller distance since it is consistent with the one derived from the Tully-Fisher relation (11.0 Mpc), which relates the rotational velocity of the galaxy to its absolute magnitude to derive its distance (Tully and Fisher, 1977). On the other hand, using a higher distance for 2014dt allows its absolute magnitudes to be much closer to SNe 2005hk and 2012z, which explains why Fox et al. (2016) chose to use a distance of 19.3 Mpc. This study will use the distance derived in Singh et al. (2018), in which the galaxy redshift is used to compute the luminosity distance:

$$D_L = (1 + z) \frac{c}{H_0} \int_0^z \frac{dz'}{E(z')}, \quad (1.1)$$

with

$$E(z) = \sqrt{\Omega_m(1+z)^3 + \Omega_k(1+z)^2 + \Omega_\Lambda} \quad (1.2)$$

Using a redshift z of 0.005224 ± 0.000007 (Binggeli et al., 1985), and the usual cosmological parameters $H_0 = 73 \pm 5 \text{ km s}^{-1} \text{ Mpc}^{-1}$, $\Omega_m = 0.27$, $\Omega_\Lambda = 0.73$ and $\Omega_k = 0$, Singh et al. (2018) estimate the luminosity distance of M61 to be $21.44 \pm 0.03 \text{ Mpc}$. This computation has a downside however, since at such small distance the redshift is comparable to any peculiar motion of the object, which could induce large errors in the result.

1.3.3 Peak Epoch

The discovery of 2014dt occurred post-peak, meaning its time of explosion and peak brightness can only be estimated. To do so, one can compare the spectral evolution to

other similar SNe spectra, using tools like Supernova Identification (SNID) (Blondin and Tonry, 2007). Another way of constraining the maximum brightness epoch is to first fit the multi-band light curves of some well studied SNe and apply this fit to the light curves of SN 2014dt. These two methods have given similar results in all studies of SN 2014dt, so this work will use the results from the latest one (Kawabata et al., 2018) in which the epoch of B-band maximum, using both methods and SNe 2005hk and 2012Z as templates, was found to be October 20.4 UT (MJD 56950.4 \pm 4.0).

1.3.4 Other SNe used in this work

Most studies of SN 2014dt, including this one, base a part of their analysis on the comparison with SNe 2005hk and 2012Z, two well-studied Type Ia.

SN 2005hk was discovered by J. Burket and W. Li (Quimby et al., 2005) on 2005 October 30.24 UT in the galaxy UGC 272 with an absolute peak brightness of -17.7 mag in the B-band. It is overall very similar to the first known Ia, 2002cx. Its early spectra are dominated by Fe III and Si II lines, while the late spectra show narrow permitted Fe II, Ca II and Na I lines instead of regular forbidden lines for Type Ia SNe. Velocities derived from the spectroscopy are low, around 6 000 $km.s^{-1}$ and its LC seem to be well explained by a Thermonuclear Explosion model (Sahu et al., 2008).

SN 2012Z was discovered on 2012 January 19.15 UT by Cenko et al. (2012) in the galaxy NGC 1309 with an absolute peak brightness of -18.3 mag in the B-band. Its near-IR LC features are very close to 2005hk, with similar peaks and decline rates, but with a faster rise. Its spectra show lines and velocities similar to 2005hk, though the lines are much broader. A possible progenitor was found by McCully et al. (2014), arguing in the favour of a CO WD accreting from a He star. The observations of SN 2012Z seem to agree with both PDD (Stritzinger et al., 2015) and failed deflagration (Yamanaka et al., 2015) explosion models.

2 The Photometry of SN 2014dt

SNe studies are based on two types of observations, their spectroscopy and their photometry. The spectroscopy of SN 2014dt is briefly presented in section 1.3 and will only be discussed in chapter 4. Its photometry, on the other hand, is investigated in this section. First, the results of the observations are summarised and compared to SNe 2005hk and 2012Z, then the bolometric luminosities of the three SNe are analysed. Finally, the Spectral Energy Distribution (SED) evolution of SN 2014dt is computed and its behaviour in the different wavelength ranges is discussed.

2.1 Observations

Since the provided data sets were already reduced, no data treatment was performed in this study. Nevertheless, the details of the observations are summarised here. The optical photometry was obtained with the Las Cumbres Observatory Global Telescope (LCOGT) Network and the Palomar 48 and 60-inch telescopes, in BVR-ri and gri filters respectively. near-IR observations were carried out in the JHK filters with the United Kingdom Infrared Telescope (UKIRT) in the Maunakea Kea Observatory. The measurements were performed with the QUBA pipeline (Valenti et al., 2011), using a DAOPHOT-based point-spread function (PSF) fitting technique and calibrated with SDSS and 2MASS stars. Template galaxy subtraction was not carried out. Mid-IR observations were made by the Spitzer Infrared Intensive Transients Survey (SPIRITS) with the two Spitzer/IRAC channels at 3.6 and 4.5 μm . Forced aperture photometry is performed for both channels after template galaxy subtraction.

2.1.1 Results

Optical, near and mid-IR Observations of SN 2014dt are shown in figure 2.1, as well the optical and near-IR light curves of SNe 2005hk and 2012Z, for comparison. As explained in section 1.3.3, SN 2014dt was discovered post-peak, so the epoch of B-band maximum, which will be taken as day 0 in this work, was estimated at MJD 56950.4 ± 4.0 . The lines show the interpolation of the magnitudes obtained with the SNPy Python module (Burns et al., 2011), using a combination of spline and polynomial fits to get the best match. The data points denoted with triangles are non-detections, the interpolations do not necessarily go through these points, but at least respect this maximum. Computed decline rates are available in table A.1.

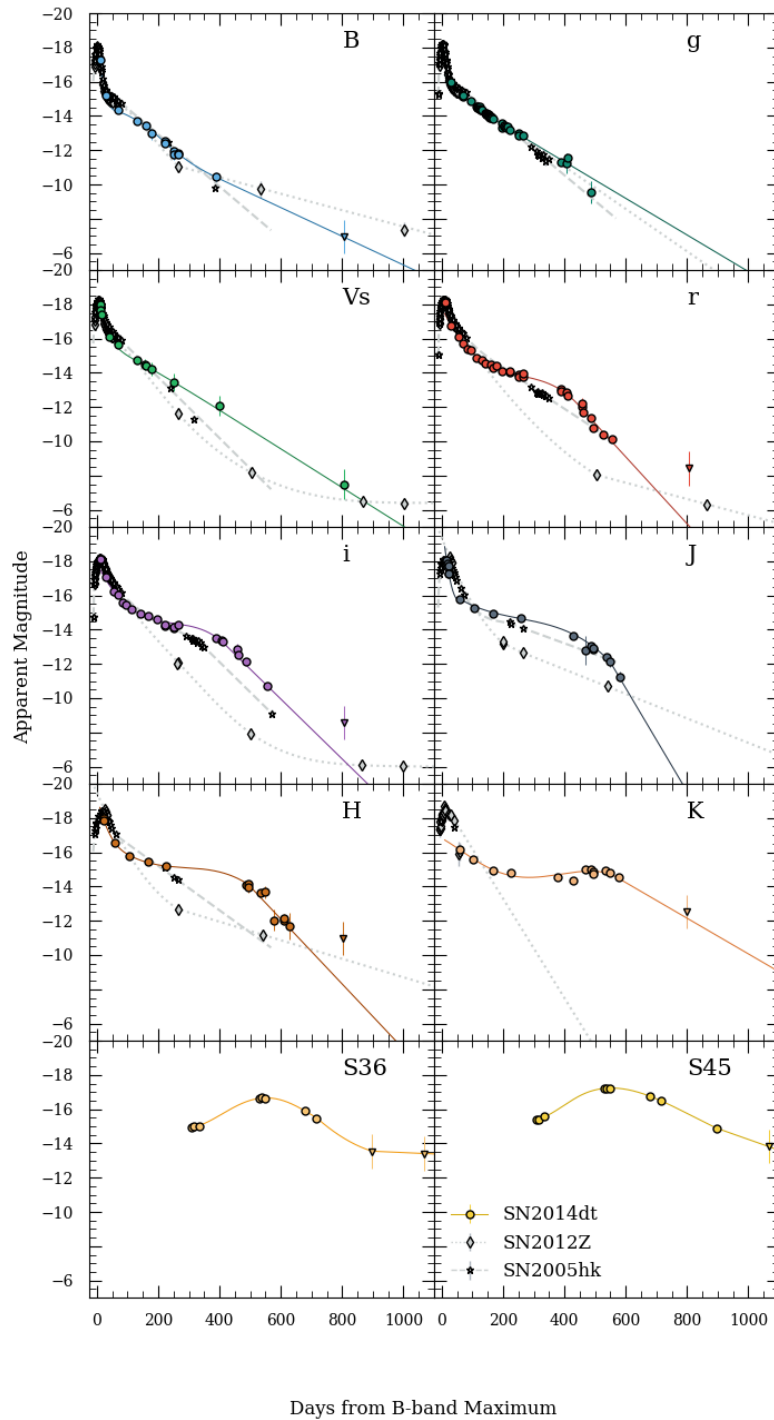


Figure 2.1: Multi-band light curves of SN 2014dt, filled circles denote the data while the lines show their interpolation. The light curves of SN2012Z and SN2005hk are plotted for comparison as triangles and stars respectively. The data points denoted with triangles are non-detections.

2.1.2 Analysis

First of all, one notes that the observations of SN 2014dt started post-maximum, which means the rising time cannot be precisely computed, and the same goes for any information that can be derived from it. Furthermore, late time near-IR data are sparser for 2005hk and 2012Z and no mid-IR observation is available, meaning no comparison will be possible in the S36 and S45 bands. Concerning the early decline rates, they are similar to SNe 2005hk and 2012Z. The brightness seems to peak and decay at approximately the same rates, which explains why SNe 2005hk and 2012Z are used as templates to find rises and peaks of 2014dt.

After 100 days, however, the shapes start to diverge. The bluer LC (BgV) differ slightly by their slope, SN 2014dt declines by around 0.01 mag/day against 0.02 mag/day for the others, but the overall shape is the same for the three SNe. On the other hand, the decline rates differ greatly when inspecting the redder wavelengths. Indeed, from red to mid-IR filters, the LC depicts a noticeable excess: around 250 days, the brightness almost plateaus in the iJHK bands, reaching declines of 0.004 mag/day, while it increases with a rate up to 0.01 mag/day in the S36 and S45 bands. In the red wavelengths (ri bands), this only occurs for 100 days, against 250-350 days for the JHK bands and more than 400 days in the S36-45 filters.

Overall, the photometry presents a significant excess of mid-IR emission compared to SNe 2005hk and 2012Z, and it contaminates the red and near-IR fluxes. The possible sources are multiple, ranging from the wind driven by a bound remnant to warm circumstellar dust. But before discussing the causes of the excess, its impact on the bolometric fluxes must be inspected.

2.2 Bolometric Light Curve

The bolometric LCs are computed from the multi-band photometry without bolometric correction. To derive the bolometric luminosity at a given time t , one must first compute the flux density in each bands from the apparent magnitudes m and the filter zero-points $f_{v,0}$ using:

$$f_v = f_{v,0} \times 10^{-m/2.5}. \quad (2.1)$$

Then one integrates f_v over the whole frequency range to get the total flux density F , which was done using the trapezoidal rule. The bolometric luminosity is then simply obtained with

$$L_{bol}(t) = 4\pi r^2 F(t), \quad (2.2)$$

where r is the distance to the object, derived in section 1.3.2.

2.2.1 Results

Figure 2.2 shows the result of this computation made with every filter available for SN 2014dt, as well as in the optical and optical + near-IR bands. The empty circles are the bolometric luminosities computed each time measurements were made in at least one band, and magnitudes in bands lacking data at that time were interpolated. The lines show the bolometric luminosity computed each day between the first and the last data points, using interpolated magnitudes. For comparison, the optical + near-IR output of SNe 2005hk and 2012Z are plotted in figure 2.3 along the near-IR LC of 2014dt. Computed decline rates are available in table A.2.

2.2.2 Analysis and Discussion

First, one notes that measurements in the S36-45 filters only start around 300 days post peak, which explains why the bolometric output computed for all filters is the same as the optical + near-IR LC before this epoch. The early phases are similar for the 3 different LCs, with slopes around $0.2 \log(\text{erg/s})/\text{day}$ at the beginning and a slower phase of $0.002 \log(\text{erg/s})/\text{day}$ between 250 and 400 days. Then the optical and optical + near-IR LCs start decreasing again at a higher rate of $0.005 \log(\text{erg/s})/\text{day}$, while the whole bolometric output continues to decline slowly at $0.003 \log(\text{erg/s})/\text{day}$.

Concerning figure 2.3, the early shape of the LCs are very similar, the decline rates all range around $0.01 \log(\text{erg/s})/\text{day}$, and although its brightness maximum was not actually observed, 2014dt seems to peak at a lower luminosity. However, the LC are strongly diverging after 100 days, as 2014dt reaches a slow decline phase that does not seem to occur for the other SNe, which are decreasing at a steady $0.005 \log(\text{erg/s})/\text{day}$ rate. In the late phase, the luminosity of 2014dt decreases at a higher rate again and the divergence from 2005hk and 2012Z is much smaller.

The comparison between the three SNe shows how the mid-IR excess in 2014dt emission affects the bolometric output. Indeed, it is likely to be responsible for the slow decline part that occurs between 300 and 600 days, which does not appear in the LCS of SNe 2005hk and 2012Z. It is worth noticing that the divergence from the two other SNe starts around 100 days post-peak, meaning the source of the excess is actually affecting the LCs much before the excess was measured. It is impossible, however, to draw any conclusion from this analysis alone. The bolometric luminosity of the SNe are strongly related to radioactive decays and γ -ray transport inside the ejecta, which means modelling such interactions is essential for understanding what drives such excess in the energy output, this is the subject of section 3. In the meantime, the SEDs must also be analysed since the excess of emission will likely to affect it, and one can use it to constrain some of the possible excess sources.

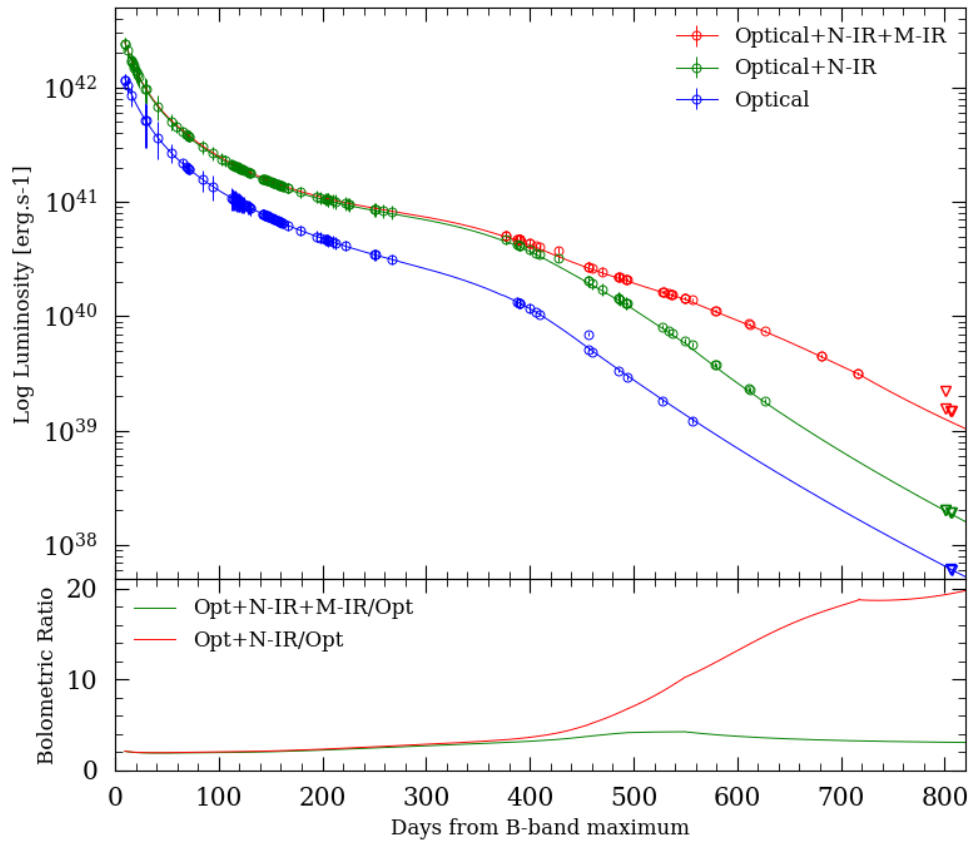


Figure 2.2: Upper panel: Bolometric light curve of SN 2014dt. The lines show luminosities derived from interpolated magnitudes. The circles show computations made each day with data in at least one filter (the data is interpolated for the filters with missing data), triangles denotes upper limits. Lower panel: Ratio between the different components of the bolometric output.

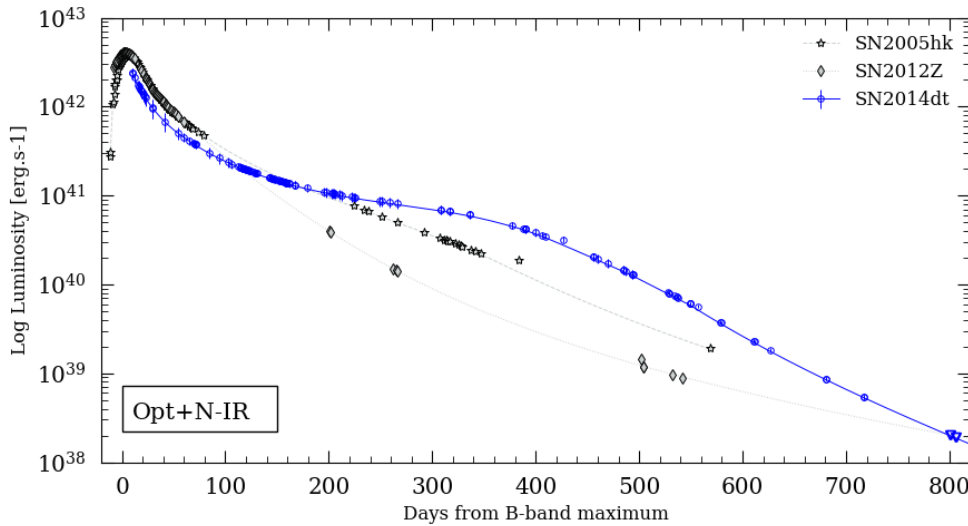


Figure 2.3: Optical + near-IR Bolometric light curve of SN 2014dt, SN2012Z and SN2005hk, triangles denotes upper limits. The lines show luminosities derived from interpolated magnitude data. The circles show computations made at each day with data in at least one filter (the data is interpolated for the filters with missing data).

2.3 Spectral Energy Distribution

The SEDs are obtained from the wavelength-dependent flux densities F_ν , which are computed from the magnitudes using equation 2.1. Then, even though SNe are not black bodies (BBs), approximating their flux densities by such an object allows to estimate their temperature and radius. The observed flux density at distance R can be obtained using $F'_\nu = \frac{r^2}{R^2} F_\nu$, with r the object radius, R the distance to the object and F_ν the flux density at its surface.

Approximating the SN as a BB, we have $F_\nu = \pi B_\nu(T_{BB})$, where $B_\nu(T_{BB})$ is the Planck function:

$$B_\nu(T) = \frac{2h\nu^3}{c^2(e^{\frac{h\nu}{k_B T}} - 1)}. \quad (2.3)$$

Therefore we can fit the observed flux using:

$$\nu F_\nu = \pi \nu B_\nu \frac{r^2}{d^2}, \quad (2.4)$$

where d is the distance to SN 2014dt computed in section 1.3.2. As such, this BB fit will be used to estimate the temperature of the SN as well as the radius of its photosphere.

2.3.1 Overall Evolution

Figure 2.4 shows the SED computed from 50 to 700 days, with 50 days intervals, and the BB fit results are reported in table 2.1. The first 300 days do not account for the S36-45 contribution since no data were available at that time.

The evolution of the BgVri-JHK bands seems regular, as the optical wavelengths contribute strongly to the SED for the first year and then their fluxes decrease sharply. The early temperature estimates seem reasonable and decrease with time, but a BB is not a good approximation for the nebular phase of a SN, which results in too high temperatures in the late phase. The BB radii have plausible values, as Kawabata et al. (2018) and Foley et al. (2016) found a radius of 2.9 and $1.3 \cdot 10^{12}$ m respectively at 410 days, using a smaller distance for 2014dt. However the evolution of the radius is unusual, as it first decreases, then increases before decreasing again. As mentioned before, the nebular phase of a SN can hardly be approximated by a BB and it could simply return wrong radii at late times. Still, such a behaviour could also be the result of an optically thick wind, meaning further investigation are required.

2.3.2 SEDs at the Epochs of IR Excess

Figure 2.5 presents the SED evolution of SN 2014dt when the excess of IR emission was observed. Since this excess was recorded around 300, 500 and 700 days, the SEDs are computed at these epochs.

The contribution of the IR wavelengths at 300 days are negligible compared to the optical part, but as the latter decreases with time, the effect of the former becomes much

more noticeable. Indeed, one can clearly see two different peaks at 500 and 700 days, indicating the presence of two bodies. To characterize them, two BB fits are performed (one for each peak), but some of the returned values are not conceivable. For the well-defined peaks, e.g. the optical body at 300 and 500 days or the mid-IR one at 500 and 700 days, the BB radius and temperature seem to match the results of section 2.3.1. On the other hand, the mid-IR and optical contributions at 300 and 700 days respectively are smaller, and the BB parameters are far off. Such results for the optical contribution is expected since no data was recorded after 600 days and these points come from interpolated magnitudes, but not for the second peak. This means the overall shape of the SED cannot be explained by two BB components, but rather one BB for the optical part and a different object for the IR emission. Finally, the temperature estimates of the second component, around 1 000 K for the reasonable ones, could be explained by warm dust. This possibility is investigated in section 4, once further analyses are carried out on the bolometric LC.

Epoch (days)	R_{BB1} (10^{12} m)	T_{BB1} (K)	R_{BB1} (10^{12} m)	T_{BB2} (K)
50	8.75	5714	-	-
100	5.41	6046	-	-
150	4.57	5813	-	-
200	4.72	5242	-	-
250	5.00	4797	-	-
350	4.86	4318	19.8	418
400	4.38	4106	30.3	836
450	3.63	3877	40.6	962
500	2.16	4108	42.5	1052
550	0.76	5360	42.0	1074
600	0.33	6805	45.9	988
650	0.24	6945	55.4	847
700	0.18	6893	65.9	723
750	0.12	6938	50.8	727
800	0.11	6945	64.9	608
850	0.09	6945	57.1	591

Table 2.1: BB Fit Parameters obtained in figure 2.3.1

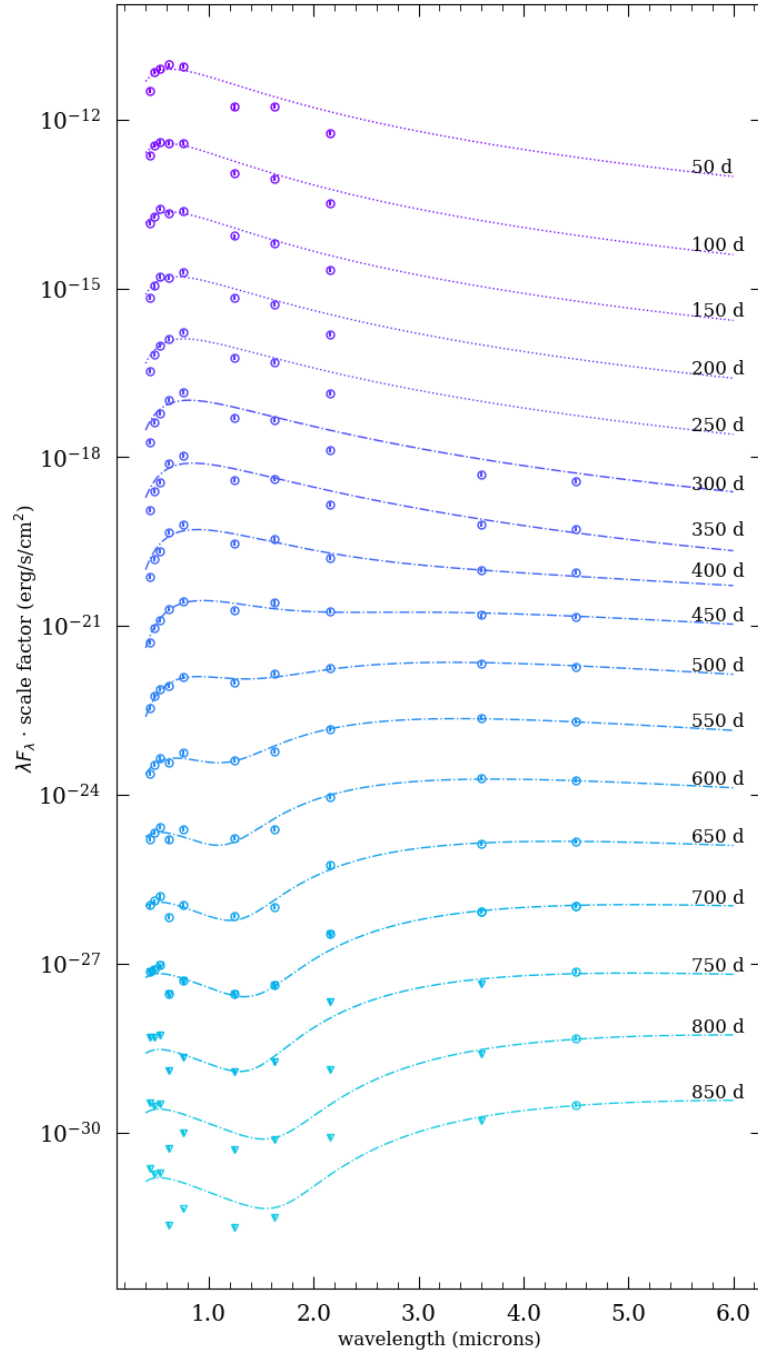


Figure 2.4: Evolution of the SED of SN 2014dt using interpolated magnitude data. The BB model fits the temperature and BB radius according to equation 2.4 and late time temperatures are forced to decrease to avoid too high values. The results are reported in table 2.1.

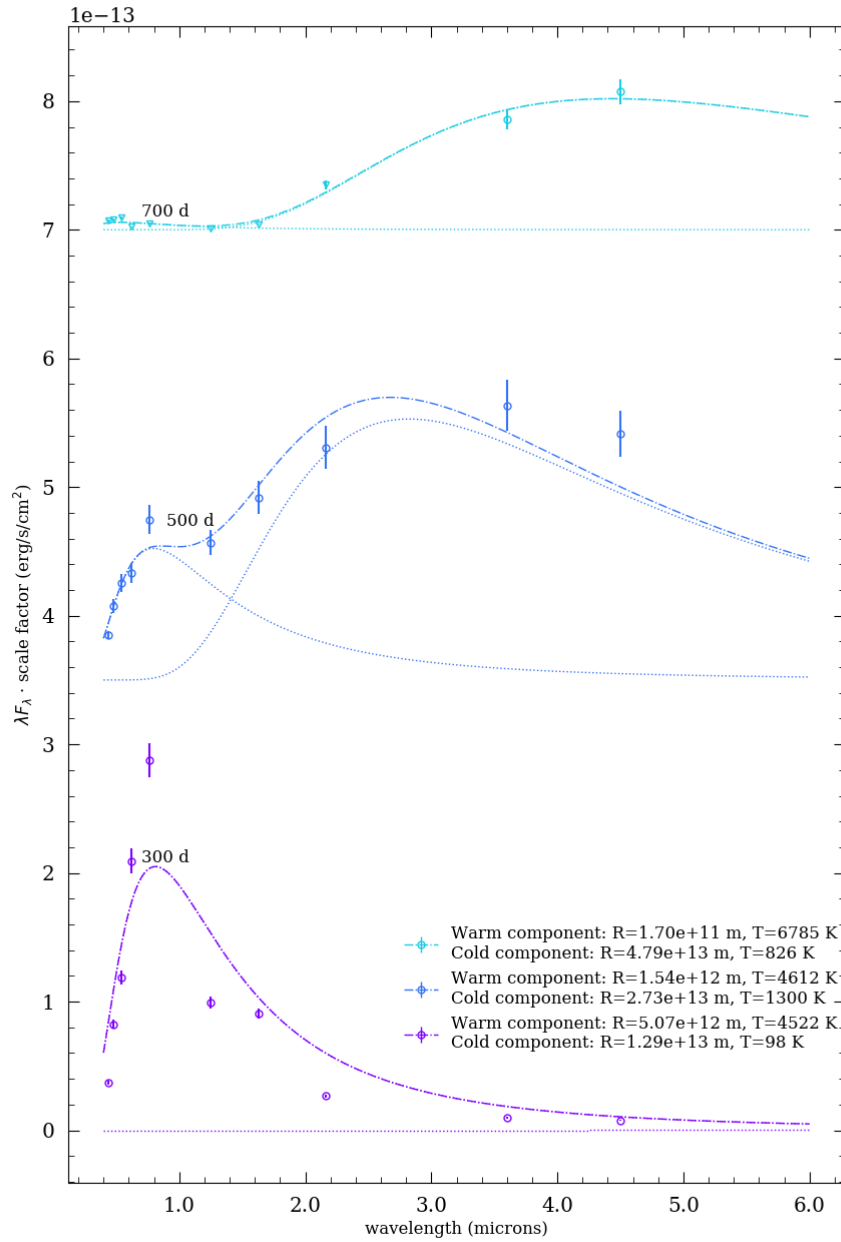


Figure 2.5: SEDs at 300, 500 and 700 days. The peaks are first fitted separately with a BB to get a guess on their parameters, then the sum of two BB is fitted over the whole SED using the initial guesses obtained before. Points denoted as triangles at 700 days are upper limits, as no observations were made in the optical + near-IR range at such epochs. The fit reports each BB temperature and radius according to equations 2.4, the results are reported in the legend.

3 The Two Component Light Curve Model

During the explosion, a Type Ia SN burns carbon and oxygen into heavier elements. The decays of these elements is responsible for the observed brightness, which means one can relate them to the shape of the bolometric LC. Studies of Type Iax make use of this kind of relation to find models that would explain their slow decline rates. This section presents the two-component LC model used by Kawabata et al. (2018), which matches early BgVri luminosities. The model is then fitted to late-time data to check if it can account for the excess of emission observed after 300 days.

3.1 Radioactive Decay and Decline Rate

Type Iax SNe are thought to mostly synthesize radioactive isotopes of Nickel and Cobalt, ^{56}Ni and ^{56}Co , triggering the decay chain $^{56}\text{Ni} \rightarrow ^{56}\text{Co} \rightarrow ^{56}\text{Fe}$. When decaying, these two elements emit γ -rays, photons with energies far outside the optical range. However, these decays occur in the inner layer of the SN, meaning the γ -rays, once emitted, start interacting with the outer, cooler layers. After going through many scattering and emission processes, some of the photons have cooled enough to have energies in the optical range. This thermalisation is responsible for the optical light emitted by the supernova. Therefore one can link the energy deposited in the ejecta by the photons from the radioactive decays to the bolometric output of the SN (Maeda et al., 2003; Kawabata et al., 2018) using the following formula:

$$L_{bol} = M(^{56}\text{Ni})[e^{-t/8.8\text{days}}\epsilon_{\gamma,\text{Ni}}(1 - e^{-\tau}) + e^{-t/113\text{days}}(\epsilon_{\gamma,\text{Co}}(1 - e^{-\tau}) + \epsilon_{e^+})], \quad (3.1)$$

with

$$\tau \simeq 1000 \times \left[\frac{(M_{ej}/M_{\odot})^2}{E_{51}} \right] (t/\text{day})^{-2} = 1000 \times \tau_0 \times (t/\text{day})^{-2} \quad (3.2)$$

Where $\epsilon_{\gamma,\text{Ni}}$ is the energy deposition rate by ^{56}Ni via γ -rays, $\epsilon_{\gamma,\text{Co}}$ and ϵ_{e^+} are the energy deposition rate by ^{56}Co via γ -rays and positron ejection, M_{ej} is the ejecta mass and $E_{51} = E_k/10^{51}$ erg.

Kawabata et al. (2018) used this model against the optical bolometric light curve of SN 2014dt from 0 to 400 days post B-band maximum and showed that it failed at describing the whole output. Indeed, while it can fit the early phase quite well, it does not reproduce the slow decrease after 60 days. Such a tail can only be matched by increasing greatly the optical depth (full trap of the γ -rays), and although the declines seem identical, it

requires a much larger bolometric luminosity in the late phase (see figure 3.1). Such results seem to point toward a two-layer structure, to account for the two phases of the decline rates.

3.2 Describing the LC With Two Components

To fit the optical output correctly, Kawabata et al. (2018) chose to work with a two-component LC model (Maeda et al., 2003), with an outer layer responsible for the early luminosities, with a small optical depth, and a denser inner layer that allows for full γ -ray trapping. Each component is described by equation 3.1, and the total optical output of the SN is defined by the sum of each output. Therefore, this model has four independent parameters, $\tau_{0,in/out}$ and $M(^{56}\text{Ni})_{in/out}$. The energy deposition rates are $\epsilon_{\gamma, Ni} = 3.9 \times 10^{10} \text{ erg} \cdot \text{s}^{-1} \cdot \text{g}^{-1}$, $\epsilon_{\gamma, Co} = 6.8 \times 10^9 \text{ erg} \cdot \text{s}^{-1} \cdot \text{g}^{-1}$ and $\epsilon_{e^+} = 2.4 \times 10^8 \text{ erg} \cdot \text{s}^{-1} \cdot \text{g}^{-1}$.

Their results are reproduced in figure 3.1 using their data set, the distance they used (14.5 Mpc) and the assumption that the optical flux is about 60% of the bolometric output. The model was fitted up to 230 days only, since later data points in Kawabata et al. (2018) were calculated using only V- and R-bands, making them rather imprecise.

The model matches the shape of the curve quite well, meaning the ejecta could be composed of two components, a dense and optically thick inner shell and an optically thinner outer shell. An optically thick and dense component sitting inside the supernova could suggest the presence of a bound remnant.

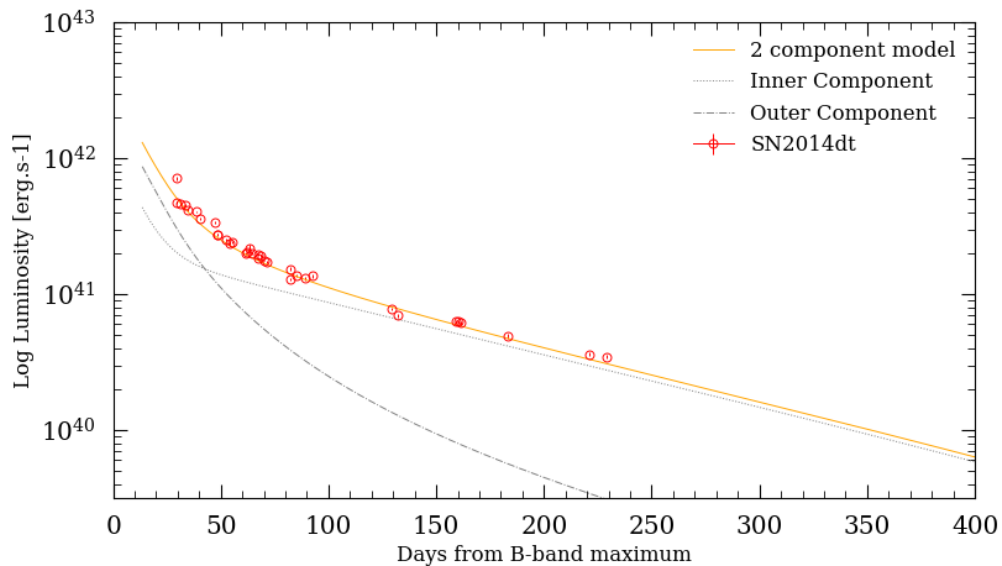


Figure 3.1: Optical Bolometric light curve of SN 2014dt using data from Kawabata et al. (2018) against the two single-component LC models (the first one to fit the early phase and the full trap to fit the tail) and two-components LC model. Parameters of the fit are listed in table 3.1.

	Best Fit		Suggested range	
	$M(^{56}\text{Ni})(M_{\odot})$	τ_0	$M(^{56}\text{Ni})(M_{\odot})$	τ_0
Inner component	0.015	500	0.015 - 0.025	≥ 500
Outer component	0.03	1.2	0.02 - 0.08	0.8 - 3.0

Table 3.1: Two Component LC parameters obtained in figure 3.1 against the range suggested by Kawabata et al. (2018).

However, the sample used here only goes up to ~ 200 - 300 days. Since an emission excess was observed around 300 days in every wavelength above the R-band, the bolometric LC decline rates change drastically from any predicted values (see section 2). It is then natural to wonder how this two-component model behaves in the presence of such emission, as well as adding data from the g-band for better precision.

3.3 Modelling the Late-Time Optical Output

3.3.1 Results

The model described in the previous section is now applied to BgVri bolometric luminosities from 0 to 800 days from B-band maximum. Figure 3.2 presents the results, and the best parameters of the model are listed in table 3.2.

The model matches the shape of the LC up to 200 days, with decline rates around $0.01 \log(\text{erg}\cdot\text{s}^{-1})\cdot\text{day}^{-1}$ for both curves, but some of the best fit parameters are not in the range obtained by Kawabata et al. (2018). After 250 days, the observed luminosities plateau to $0.0015 \log(\text{erg}\cdot\text{s}^{-1})\cdot\text{day}^{-1}$ then decrease at a regular pace of $0.003 \log(\text{erg}\cdot\text{s}^{-1})\cdot\text{day}^{-1}$, while the model continuously declines at around $0.005 \log(\text{erg}\cdot\text{s}^{-1})\cdot\text{day}^{-1}$. In the latest phase, the decline rates finally match but the model actually predicts a much lower output.

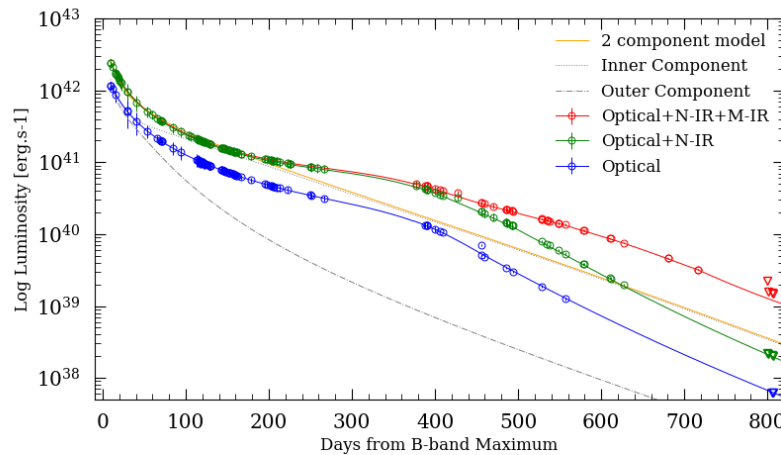


Figure 3.2: Optical, near and mid-IR Bolometric light curve of SN 2014dt against the two components LC model (see eq. 3.1), triangles denotes upper limits. The values for the free parameters of the model are given in table 3.1.

	Parameters from figure 3.2		Suggested range	
	$M(^{56}\text{Ni})(M_{\odot})$	τ_0	$M(^{56}\text{Ni})(M_{\odot})$	τ_0
Inner component	0.037	1000	0.015 - 0.025	≥ 500
Outer component	0.032	3.32	0.02 - 0.08	0.8 - 3.0

Table 3.2: Two Component LC parameters obtained in figure 3.2 against the range suggested by Kawabata et al. (2018).

3.3.2 Discussion

First of all, one notes that it was very unlikely for the model to match the shape caused by the excess. The divergence from the observations starts around the same epoch as the end of the data sample used by Kawabata et al. (2018), which explains why the fit of this model might have seen reasonable. While it could probably predict the LCs of SNe 2012z and 2005hk, the divergence of 2014dt from standard Iax LCs is too strong to be explained by regular γ -ray transport only.

Concerning the parameters of the best fit, both components tend to slightly diverge from the suggested range. One notes that the early data distribution from Kawabata et al. (2018) looks slightly random, as some sets of measurements were obtained in short time intervals with large brightness variations, while early data from this work seem to be more smoothly distributed. Furthermore, data from figure 3.1 and 3.2 begin around 20 days and 10 from B-band maximum respectively, meaning the second one shows data closer to the peak, with higher decline rates. This two factors could lead to a different shape and explain the discrepancy between the component parameters.

The model predicts the Ni mass to be around $0.07 M_{\odot}$, which is conceivable considering SN 2014dt is not very luminous. It is also in the mass range suggested by Kawabata et al. (2018), 0.04 - $0.10 M_{\odot}$, which was estimated using rising times. Although since no measurements were made before the peak, the rising times needed to be estimated by comparison with SNe 2005hk and 2012z, which greatly increases the uncertainties on the mass estimation.

Overall, the two-component model fails to predict the correct optical output mainly because of the plateau that occurs between 250 and 400 days, meaning this shape is not caused by the radioactive decays inside the SN. However, apart from this specific part of the LC, it looks like the model might be able to match the curve. Indeed, the early phase is explained perfectly by the decays, and while the late phase seems to significantly diverge from the observations, the very late decline rates are very much alike. This could mean that without the observed excess in red and IR wavelength, the two-component LC model would actually work. This would also imply that the source of these peculiar emissions could be a separate body, e.g. some unbound material surrounding the SN.

Finally, the results of this model do not contradict nor confirm the Pure Deflagration model with a bound remnant. Since a remnant would probably accrete material from the ejecta, and the resulting fall-back would have an impact on the luminosities, further

modelling of the bolometric LC is needed to conclude on this matter.

The source of this excess could be a separate body and does not involve radioactive decay. Since the excess is observed in IR-bands, it could possibly involve warm dust, and if so, its impact and properties can be derived from the second peaks previously observed in the SEDs.

4 Warm Dust

The excess observed in the mid-IR could be explained by circumstellar dust around the SN. As discussed in section 2, the SEDs of SN 2014dt suggest the presence of two components. Indeed, after 300 days the curves describe two different peaks, and while the first can be approximated by a BB, the second shape could be explained by warm dust surrounding the SN. Moreover, as shown in figure 4.1, SN 2014dt seems to lie in some sort of intermediate state between the Normal Ia and Ia-CSM groups, which could indicate by the presence of dust.

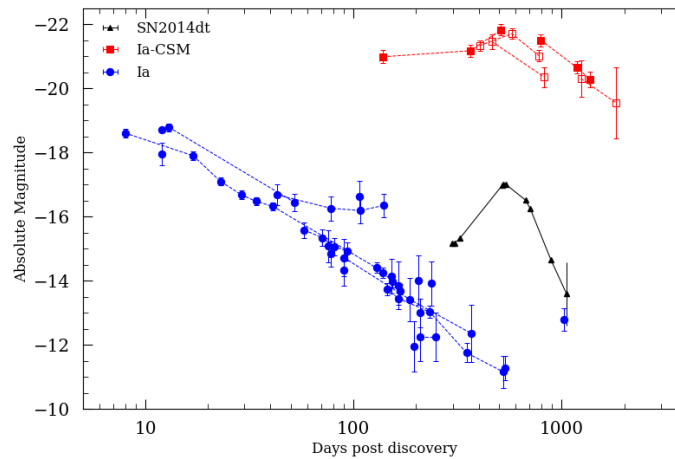


Figure 4.1: Comparison of 2014dt absolute magnitude obtained with Spitzer $4.5\mu\text{m}$ channel to other Ia and Ia-CSM SNe.

In order to determine if warm dust could be responsible for the observed excess, its temperature and mass are computed from the SEDs. The dust could then be newly formed or have existed before the explosion. The second case is considered in this work, and since the dust needs to be heated to reach the observed temperature, the dust parameters are tested against possible heating mechanisms such as radiative and shock heating.

4.1 Dust Model

The flux density F_ν of an optically thin dust cloud is given by a modified BB (Hildebrand, 1983):

$$F_\nu = \frac{M_d B_\nu(T_d) \kappa_\nu(a)}{d^2}, \quad (4.1)$$

with the dust mass M_d , the Planck function B_ν , the dust temperature T_d , the distance to the cloud d , spherical dust grains of radius a and the dust absorption coefficient κ_ν , given by:

$$\kappa_\nu(a) = \frac{3Q_\nu(a)}{4a\rho} \quad (4.2)$$

Here, $Q_\nu(a)$ is the emission efficiency factor, which depends on the grain radius as shown in figure 4.2, and ρ is the dust bulk density.

4.1.1 Results

The flux densities computed in section 2 are fitted with equation 4.1 using graphitic dust (Draine and Lee, 1984) and a dust bulk density of 2.3 gm^3 . The size of the dust grain is chosen using figure 4.2: a size of $1.0 \mu\text{m}$ or above does not have much impact on the mid-IR flux, so the grain radius should be lower than this limit. Since most similar studies use a size of $0.1 \mu\text{m}$ (Szalai et al., 2019), the same choice is made here to allow for comparisons.

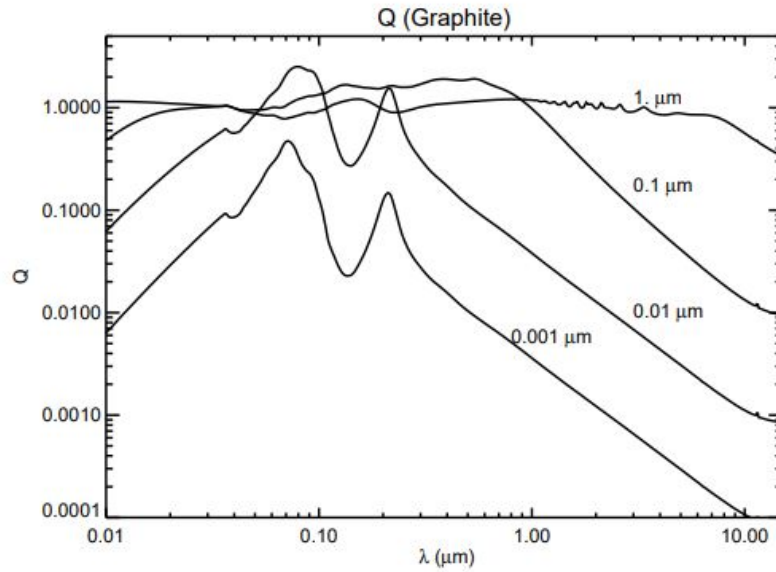


Figure 4.2: Evolution of the emission efficiency factor depending on the grain radius. Figure from Fox et al. (2010).

Two different components are fitted to the whole SED, a BB for the first peak and warm dust for the second one. Figure 4.3 presents the model applied at 300, 500 and 700 days, and the resulting parameters are listed in table 4.1.

The model at 300 days does not match all the data, the measurements in the ri-bands are more than twice as large as the other points, and the mid-IR fluxes are low compared to the rest of the observations. On the other hand, the parameters it returns agree with results from section 2. At 500 days, which is around the peak of mid-IR excess, the fit behaves well and follows the two peaks closely, and the values returned by the model match previous estimations. Finally, at 700 days, the overall observations agree with

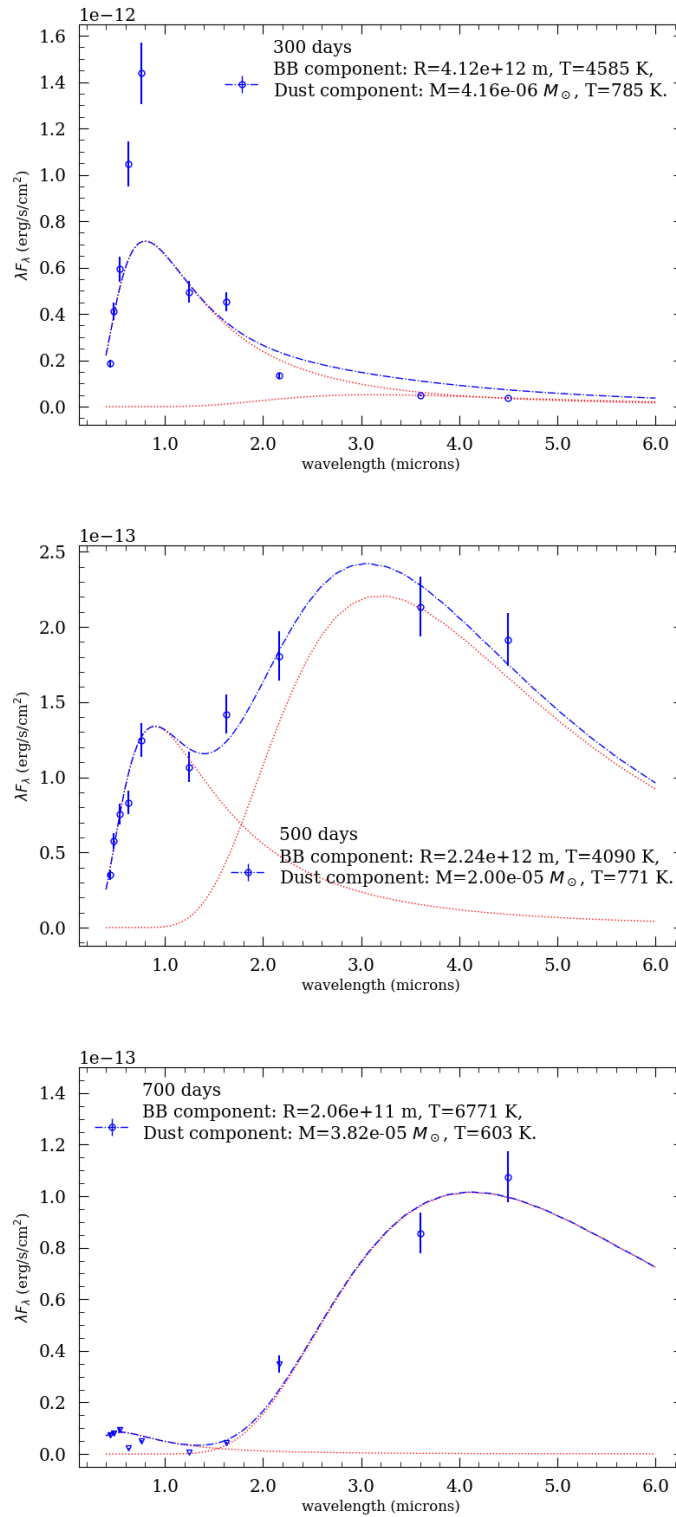


Figure 4.3: Fit of the SED at 300, 500 and 700 days with a BB for the first peak and warm dust for the second one. The peaks are first fitted separately to get an initial guess on their parameters, then the sum of the two models is fitted to the whole SED using the initial guesses obtained before. Points denoted as triangles at 700 days are upper limits, as no observations were made in the optical + near-IR range at such epochs. The fit reports each component temperature and mass according to equations 4.1 and 2.4, the results are reported in table 4.1.

the prediction, but since the values in the optical + near-IR range are only upper limits obtained with the interpolation of the photometry, the BB parameters reported by the fit are slightly off.

BB Fit		
Epoch (days)	R_{BB} (m)	T_{BB} (K)
300	4.12×10^{12}	4585
500	2.24×10^{12}	4090
700	2.06×10^{11}	6771
Dust Fit		
Epoch (days)	M_d (M_{\odot})	T_d (K)
300	4.16×10^{-6}	785
500	2.00×10^{-5}	771
700	3.82×10^{-5}	603

Table 4.1: Black body and dust fit Parameters

Further efforts are needed to confirm the dust hypothesis. Since only one dust composition was considered here, one needs to use the model with different dust grains, such as amorphous carbon or silicate. Moreover, a specific grain size was used here, meaning there is a whole range of grain radii left to test.

4.1.2 Discussing the Spectroscopy

While the BB fit does not always return conceivable parameters, the dust fit seems to be relatively on point. Further analysis can be done by inspecting the spectroscopy of SN 2014dt for peculiar lines indicating the presence of dust. No such study is done in this work, however, a brief overview of the optical + HK spectra around 550 days along with the SED is given in figure 4.4. The optical and H-band spectra match astonishingly well the shape of the SED, and rapid inspection of the H-band spectrum reveals a narrow Fe II emission line around $1.65 \mu\text{m}$. The full width at half maximum of this peak gives a velocity of $\sim 1\,000 \text{ km} \cdot \text{s}^{-1}$, which is very low even for a Type Iax SN ejecta. Although a more thorough analysis is required to make any conclusion, this would indicate the presence of a post-shocked CSM. Furthermore, while the K-band spectrum does not follow the SED trend, it still holds valuable information, as it includes wavelengths where CO lines might appear. Since CO molecules contributes greatly to the cooling of the ejecta, their presence seems to be a prerequisite for dust formation (Banerjee et al., 2018). Figure 4.5 shows the K-band spectrum with the mentioned CO lines, which could correspond to the observed peaks between 2.25 and $2.40 \mu\text{m}$. However, as seen in early near-IR spectra of the Iax SN 2014ck, these emissions could also be identified as Co II lines (Tomasella et al., 2016). While further analysis is needed, this spectrum could

suggest the presence of CO emission, which in turn could confirm the presence of dust surrounding SN 2014dt.

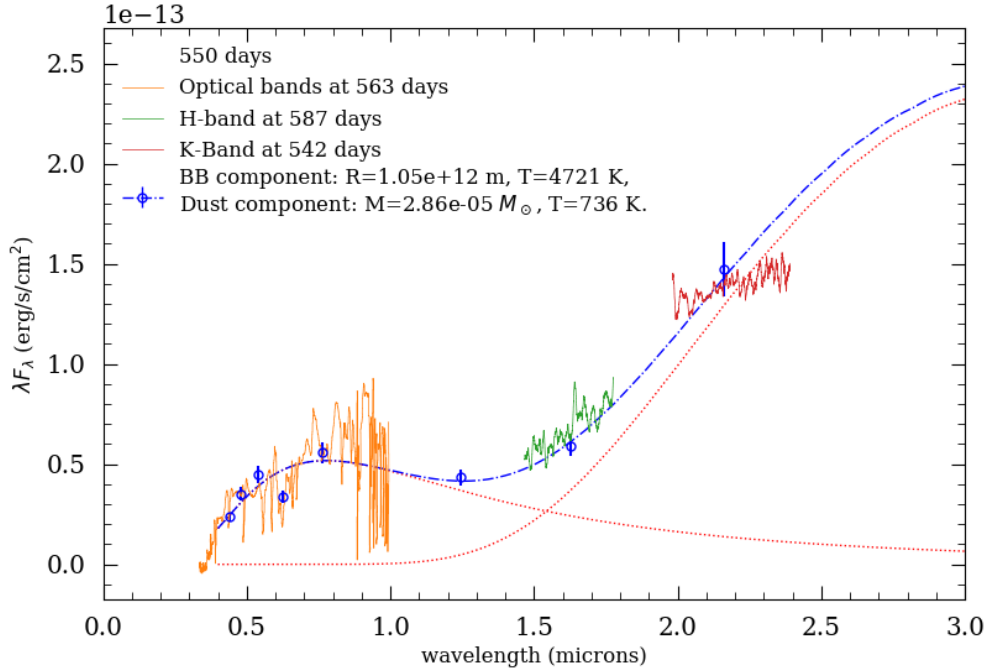


Figure 4.4: Fit of the SED at 550 days with a BB for the first peak and dust for the second one, with scaled optical, H and K-bands spectroscopy overplotted. The spectra are corrected for a redshift of 0.005224 and smoothed using a Savitzky-Golay filter.

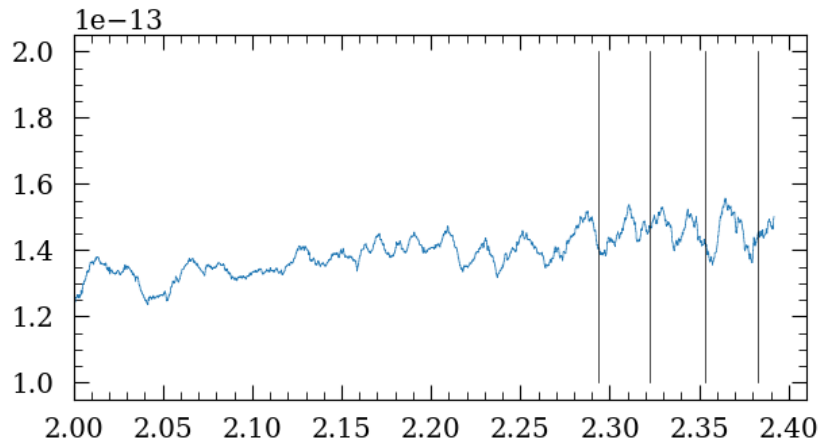


Figure 4.5: Spectroscopy of SN 2014dt at 542 days between 2 and 2.4 μm along with $^{12}\text{C}^{14}\text{O}$ lines. The spectrum is corrected for a redshift of 0.005224 and smoothed using a Savitzky-Golay filter.

Overall, the dust model seems to describe the near to mid-IR contributions really well. It predicts $\sim 10^{-5} M_{\odot}$ of dust at a temperature of 700 K, but further constraining is needed, as nothing is known about its origin and heating mechanism.

4.2 Heating Mechanism

This dust may have existed before the SN, in the form of a dusty CSM, or it may be newly formed, e.g. by condensation in the SN ejecta or the post-shock environment. Depending on when it formed, the mechanisms responsible for its temperature are different, which means testing different heating scenarios and ruling them out allows for more constraints on the dust characteristics. Concerning pre-existing dust, two heating scenarios can be considered, radiative heating and shock heating.

4.2.1 Radiative Heating

A dust shell sitting at a certain distance from the SN can be radiatively heated by its peak luminosity. However, light travel times affect the perception of the thermal radiation, leading to a phenomenon called "IR Echo". Thanks to this echo, it is possible to predict the temperature of radiatively heated dust using the SN photometry. First, one can find the size of the dust shell using a simple geometrical argument:

$$r_{shell} = \frac{ct_{peak}}{2}, \quad (4.3)$$

where c is the speed of light. The obtained dust radius can then be used together with the peak luminosity of the SN and the dust grain size to estimate the dust temperature (see section 8.2.3 in Krügel (2003)) :

$$T_{dust} = 4.0 \cdot \left(\frac{L_{max}}{a} \right)^{1/6} \cdot r_{dust}^{-1/3}, \quad (4.4)$$

with a and r_{dust} in cm and L_{max} in $\text{erg} \cdot \text{s}^{-1}$. This reasoning is now applied to SN 2014dt: with a peak of mid-IR emission occurring around 500 days post peak, the dust shell radius is $\sim 6.5 \cdot 10^{15}$ m. Since the luminosity maximum was not observed, an upper limit of $3.0 \cdot 10^{42} \text{ erg} \cdot \text{s}^{-1}$ is used along a grain size of $0.1 \mu\text{m}$ and the previously computed radius to obtain a dust temperature of ~ 378 K. This means that dust emitting thermal radiations equivalent to the IR excess observed in SN 2014dt photometry would only have a temperature around 400 K. Therefore, radiative heating does not seem to be efficient enough to explain the temperatures predicted by the dust model in section 4.1.1. However, both the dust model and the radiative heating process are dependent on the dust grain size, meaning this mechanism is only ruled out for a specific set of parameters. This degeneracy can be lifted either by using some constraints on the grain radius or by testing this process against a whole range of radius instead of just one. Since no such constraints were yet deduced from observations, further tests of radiative heating are needed to fully rule it out.

4.2.2 Shock Heating

Alternatively, pre-existing dust could be heated by collisions with hot electron gas after the forward shock of the SN. The mass of gas processed by the forward shock of the supernova can be approximated by (Fox et al., 2010):

$$M_g \approx 8.3 \cdot 10^{-7} \left(\frac{v_s}{1000 \text{ km} \cdot \text{s}^{-1}} \right)^3 \left(\frac{t}{\text{year}} \right)^2 \left(\frac{a}{\mu\text{m}} \right), \quad (4.5)$$

where v_s is the speed of the forward shock and a is the grain size. Using a dust-to-gas ratio of 0.01, the amount of dust processed by the forward shock is then estimated and plotted in figure 4.6 for $v_s = 5000 \text{ km} \cdot \text{s}^{-1}$ and $v_s = 15000 \text{ km} \cdot \text{s}^{-1}$, along with the dust masses obtained in section 4.1.1 and some Type Ia-CSM dust masses for comparison.

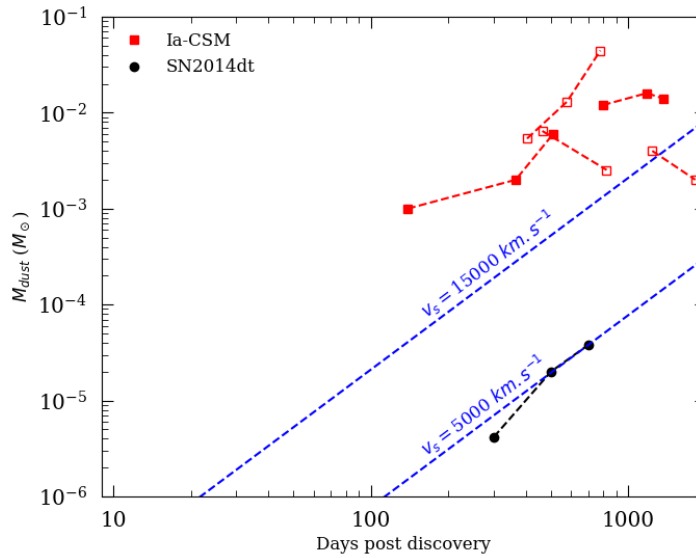


Figure 4.6: Dust masses obtained from fitting the SEDs at different epochs. The blue lines are the theoretical masses of dust shocked at velocities $v_s = 5000 \text{ km} \cdot \text{s}^{-1}$ and $v_s = 15000 \text{ km} \cdot \text{s}^{-1}$ (see equation 4.5). Type Ia-CSM supernovae data are plotted as squares, empty ones corresponds to upper limits. Dust parameters for SN 2014dt are listed in table 4.1.

First of all, one can see that the Ia-CSM masses are much larger than the dust mass of SN 2014dt, which explains the difference in mid-IR emission between the two types of SNe shown in figure 4.1. Concerning the shock velocities, while the masses processed by a $v_s = 15000 \text{ km} \cdot \text{s}^{-1}$ shock are higher than the 2014dt dust masses, the $v_s = 5000 \text{ km} \cdot \text{s}^{-1}$ shock actually predicts very similar masses, meaning such a shock could explain the observed dust temperature.

As a quick check, one can compute how much time such a forward shock should take to reach the dust shell if its inner radius is around the radius of evaporation, r_{evap} , of the SN. The evaporation radius, below which dust grains cannot survive, can be found using equation 4.4, in which T_{dust} is set to the evaporation temperature of graphitic dust (2000 K). Using the resulting radius $r_{\text{evap}} \sim 4.4 \cdot 10^{15} \text{ cm}$, a forward shock propagating at

$v_s = 5\,000\text{ km} \cdot \text{s}^{-1}$ takes ~ 100 days to reach the lower boundaries of the region where dust can sit. Since the IR excess starts ~ 300 days post peak, this result agrees with the observations made in figure 4.6.

While the shock hypothesis seems to agree with the observations, the hot electron gas still need constraining. For that matter, one can use figure 4.7, which shows that a dust at 700 K requires an electron density above $\sim 10^6\text{ cm}^{-3}$, but the analysis cannot go much further since observations and constraints on the electron plasma are lacking. This figure still provides valuable insight, as the predicted plasma should be dense enough to leave imprints on SN 2014dt radio and X-ray emission. The study of such emission would be the next step in constraining the shock heating scenario, however, no such observations are available for now.

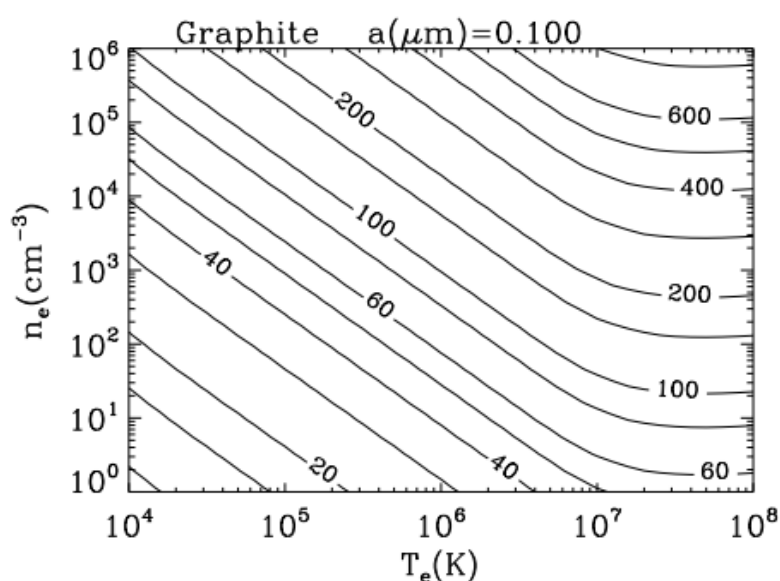


Figure 4.7: Post-shock dust temperature as a function of post-shock electron gas temperature, T_e (K), and density n_e (cm^{-3}) with a $0.1\text{ }\mu\text{m}$ graphitic dust. Plot from Fox et al. (2010).

Ultimately, the shock heating scenario cannot be ruled out, as further constraining is necessary. Radiative heating, on the other hand, does not seem efficient enough to account for such temperatures, but it still needs to be tested with different dust parameters. These two scenarios only consider pre-existing dust, meaning one still needs to constrain the newly-formed dust scenario and the heating mechanism that go along with it.

5 Conclusion

This work presented optical to mid-IR photometry of SN 2014dt up to 3 years post-explosion. The near and mid-IR observations show a clear excess of emission between 300 and 700 days, which has never been observed for a Type Iax SN. LC comparisons between SN 2014dt, SNe 2005hk and 2012Z show obvious divergences around the period of the IR excess, during which the luminosity of 2014dt plateaus instead of declining at a regular rate. Moreover, during the excess epoch the SED of 2014dt seem to be composed of two distinct bodies: one in the optical range that is well described with a BB, and another one in the near and mid-IR range that cannot be described with a BB, but seem to have a temperature around 1 000 K.

The bolometric LC of SN 2014dt was tested against a two-component radioactive LC model, describing two layers of ejecta differing by their ^{56}Ni densities and optical depth. This model was successfully applied to data up to 250 days post-peak, yielding a dense inner component allowing for the full trap of γ -rays, and a lighter and optically thin outer component. However, it fails to describe the LC at later times, as it is unable to predict the shape of the excess between 250 and 400 days. One notes that it might be able to match the overall shape of the LC if no excess was present. This could indicate that an object independent of the SN is responsible for the mid-IR emission, like a warm dust shell. Nonetheless, further modelling of the LC is needed to constrain this hypothesis, as the bound remnant predicted by some explosion models could also cause a divergence from regular emission. Indeed, the remnant would accrete surrounding material which would induce a fall-back and possibly impact the output of the SN.

The excess of mid-IR emission could also be caused by a warm dust shell sitting around the SN. Such an object can be modelled using several dust properties: with graphitic dust and a grain size of $0.1\ \mu\text{m}$, the SED was successfully described by $10^{-5}\ M_{\odot}$ of warm dust at $\sim 700\ \text{K}$. This result could be confirmed by spectral analysis in the near to mid-IR wavelengths, as the spectra of 2014dt around 550 days show potential CO emission lines. Heating mechanisms are then constrained for a pre-existing dust scenario. Radiative heating is not efficient enough, it can only heat dust up to $\sim 400\ \text{K}$ at the dust radius defined by the IR echo caused by the thermal radiations, though testing with different dust parameters is required. Shock heating seem to predict the correct amount of heated dust, and therefore is not ruled out. However it requires constraints on the hot electron gas involved in the collisions, which could potentially be obtained from observations in other wavelength ranges.

The results of this study seem to point towards the existence of warm dust surrounding SN 2014dt. While it explains the observed mid-IR excess quite well, more constraints

on its origin are needed, as only a pre-existing dusty CSM with a specific set of dust parameters was considered in this work, and some of the heating mechanisms still require further constraining. In particular, X-ray and radio observations could shed some light on some of the hypotheses. More advanced modelling of the bolometric LC is also necessary, since some components of the SN, like a bound remnant, might be able to account for the excess of emission. When coupled with a thorough analysis of the late time spectra, the advanced study of both the bolometric LC and the dust hypothesis will give useful insights on the nature of the progenitor system and the physical processes occurring inside the SN.

Literature

- Banerjee, D. P. K., Joshi, V., Evans, A., Srivastava, M., Ashok, N. M., Gehrz, R. D., Connelley, M. S., Geballe, T. R., Spyromilio, J., and Rho, J. (2018). Early formation of carbon monoxide in the Centaurus A supernova SN 2016adj. *Mon. Not. Roy. Astron. Soc.*, 481(1):806–818.
- Binggeli, B., Sandage, A., and Tammann, G. A. (1985). Studies of the Virgo Cluster. II - A catalog of 2096 galaxies in the Virgo Cluster area. *The Astronomical Journal*, 90:1681–1759.
- Blondin, S., Matheson, T., Kirshner, R. P., Mandel, K. S., Berlind, P., Calkins, M., Challis, P., Garnavich, P. M., Jha, S. W., Modjaz, M., Riess, A. G., and Schmidt, B. P. (2012). The Spectroscopic Diversity of Type Ia Supernovae. *The Astronomical Journal*, 143:126.
- Blondin, S. and Tonry, J. L. (2007). Determining the type, redshift, and age of a supernova spectrum. *The Astrophysical Journal*, 666(2):1024–1047.
- Burns, C. R., Stritzinger, M., Phillips, M. M., Kattner, S., Persson, S. E., Madore, B. F., Freedman, W. L., Boldt, L., Campillay, A., Contreras, C., Folatelli, G., Gonzalez, S., Krzeminski, W., Morrell, N., Salgado, F., and Suntzeff, N. B. (2011). The Carnegie Supernova Project: Light-curve Fitting with SNooPy. *The Astronomical Journal*, 141:19.
- Cenko, S. B., Li, W., Filippenko, A. V., Brimacombe, J., Meyer, S., Emig, K., Kaleida, C., Mamajek, E. E., Cohen, D. P., Silverman, J. M., and Ganeshalingam, M. (2012). Supernova 2012Z in NGC 1309 = Psn J03220535-1523156. *Central Bureau Electronic Telegrams*, 3014.
- Draine, B. T. and Lee, H. M. (1984). Optical properties of interstellar graphite and silicate grains. *The Astrophysical Journal*, 285:89–108.
- Foley, R. J., Challis, P. J., Chornock, R., Ganeshalingam, M., Li, W., Marion, G. H., Morrell, N. I., Pignata, G., Stritzinger, M. D., Silverman, J. M., Wang, X., Anderson, J. P., Filippenko, A. V., Freedman, W. L., Hamuy, M., Jha, S. W., Kirshner, R. P., McCully, C., Persson, S. E., Phillips, M. M., Reichart, D. E., and Soderberg, A. M. (2013). Type Iax Supernovae: A New Class of Stellar Explosion. *The Astrophysical Journal*, 767(1):57.
- Foley, R. J., Jha, S. W., Pan, Y.-C., Zheng, W., Bildsten, L., Filippenko, A. V., and Kasen, D. (2016). Late-time Spectroscopy of Type Iax Supernovae. *Mon. Not. Roy. Astron. Soc.*, 461(1):433–457.
- Foley, R. J., Van Dyk, S. D., Jha, S. W., Clubb, K. I., Filippenko, A. V., Mauerhan, J. C., Miller, A. A., and Smith, N. (2015). On the Progenitor System of the Type Iax Supernova 2014dt in M61. *The Astrophysical Journal*, 798(2):L37.
- Fox, O. D., Chevalier, R. A., Dwek, E., Skrutskie, M. F., Sugerman, B. E. K., and Leisenring, J. M. (2010). Disentangling the Origin and Heating Mechanism of Supernova Dust: Late-time Spitzer Spectroscopy of the Type IIn SN 2005ip. *The Astrophysical Journal*, 725(2):1768–1778.
- Fox, O. D., Johansson, J., Kasliwal, M., Andrews, J., Bally, J., Bond, H. E., Boyer, M. L., Gehrz, R. D., Helou, G., Hsiao, E. Y., Masci, F. J., Parthasarathy, M., Smith, N., Tinyanont, S., and van Dyk, S. D. (2016). An excess of mid-infrared emission from the type iax sn 2014dt. *The Astrophysical Journal*, 816(1):L13.
- Hildebrand, R. H. (1983). The Determination of Cloud Masses and Dust Characteristics from Submillimetre Thermal Emission. *Quarterly Journal of the Royal Astronomical Society*, 24:267.

- Jha, S. W. (2017). *Type Iax Supernovae*, page 375. Springer International Publishing AG.
- Kawabata, M., Kawabata, K. S., Maeda, K., Yamanaka, M., Nakaoka, T., Takaki, K., Fukushima, D., Kojiguchi, N., Masumoto, K., Matsumoto, K., Akitaya, H., Itoh, R., Kanda, Y., Moritani, Y., Takata, K., Uemura, M., Ui, T., Yoshida, M., Hattori, T., Lee, C.-H., Tominaga, N., and Nomoto, K. (2018). Extended optical/nir observations of type iax supernova 2014dt: Possible signatures of a bound remnant. *Publications of the Astronomical Society of Japan*, 70(6):91474O.
- Krügel, E. (2003). *The physics of interstellar dust*. CRC Press.
- Li, W. et al. (2003). Sn 2002cx: the most peculiar known type ia supernova. *Publ. Astron. Soc. Pac.*, 115:453–473.
- Maeda, K., Mazzali, P. A., Deng, J., Nomoto, K., Yoshii, Y., Tomita, H., and Kobayashi, Y. (2003). A two-component model for the light curves of hypernovae. *The Astrophysical Journal*, 593(2):931–940.
- McCully, C., Jha, S. W., Foley, R. J., Bildsten, L., Fong, W.-f., Kirshner, R. P., Marion, G. H., Riess, A. G., and Stritzinger, M. D. (2014). A luminous, blue progenitor system for a type-Iax supernova. *Nature*, 512:54.
- Nakano, S., Itagaki, K., Guido, E., Nicolini, M., Howes, N., Kiyota, S., Masi, G., Catalano, P., Vagnozzi, A., and Munari, U. (2014). Supernova 2014dt in M61 = Psn J12215757+0428185. *Central Bureau Electronic Telegrams*, 4011.
- Ochner, P., Tomasella, L., Benetti, S., Cappellaro, E., Elias-Rosa, N., Pastorello, A., and Turatto, M. (2014). Supernova 2014dt in M61 = Psn J12215757+0428185. *Central Bureau Electronic Telegrams*, 4011.
- Parrent, J. T., Howell, D. A., Friesen, B., Thomas, R. C., Fesen, R. A., Milisavljevic, D., Bianco, F. B., Dilday, B., Nugent, P., Baron, E., Arcavi, I., Ben-Ami, S., Bersier, D., Bildsten, L., Bloom, J., Cao, Y., Cenko, S. B., Filippenko, A. V., Gal-Yam, A., Kasliwal, M. M., Konidaris, N., Kulkarni, S. R., Law, N. M., Levitan, D., Maguire, K., Mazzali, P. A., Ofek, E. O., Pan, Y., Polishook, D., Poznanski, D., Quimby, R. M., Silverman, J. M., Sternberg, A., Sullivan, M., Walker, E. S., Xu, D., Buton, C., and Pereira, R. (2012). Analysis of the Early-time Optical Spectra of SN 2011fe in M101. *The Astrophysical Journal Letters*, 752:L26.
- Pereira, R., Thomas, R. C., Aldering, G., Antilogus, P., Baltay, C., Benitez-Herrera, S., Bongard, S., Buton, C., Canto, A., Cellier-Holzem, F., Chen, J., Childress, M., Chotard, N., Copin, Y., Fakhouri, H. K., Fink, M., Fouchez, D., Gangler, E., Guy, J., Hillebrandt, W., Hsiao, E. Y., Kerschhaggl, M., Kowalski, M., Kromer, M., Nordin, J., Nugent, P., Paech, K., Pain, R., Pécontal, E., Perlmutter, S., Rabinowitz, D., Rigault, M., Runge, K., Saunders, C., Smadja, G., Tao, C., Taubenberger, S., Tilquin, A., and Wu, C. (2013). Spectrophotometric time series of SN 2011fe from the Nearby Supernova Factory. *Astronomy & Astrophysics*, 554:A27.
- Phillips, M. M., Li, W., Frieman, J. A., Blinnikov, S. I., DePoy, D., Prieto, J. L., Milne, P., Contreras, C., Folatelli, G., Morrell, N., Hamuy, M., Suntzeff, N. B., Roth, M., González, S., Krzeminski, W., Filippenko, A. V., Freedman, W. L., Chornock, R., Jha, S., Madore, B. F., Persson, S. E., Burns, C. R., Wyatt, P., Murphy, D., Foley, R. J., Ganeshalingam, M., Serduke, F. J. D., Krisciunas, K., Bassett, B., Becker, A., Dilday, B., Eastman, J., Garnavich, P. M., Holtzman, J., Kessler, R., Lampeitl, H., Marriner, J., Frank, S., Marshall, J. L., Miknaitis, G., Sako, M., Schneider, D. P., van der Heyden, K., and Yasuda, N. (2007). The Peculiar SN 2005hk: Do Some Type Ia Supernovae Explode as Deflagrations? *The Publications of the Astronomical Society of the Pacific*, 119:360–387.
- Phillips, M. M., Lira, P., Suntzeff, N. B., Schommer, R. A., Hamuy, M., and Maza, J. (1999). The Reddening-Free Decline Rate Versus Luminosity Relationship for Type IA Supernovae. *The Astronomical Journal*, 118:1766–1776.
- Quimby, R., Hoeflich, P., Kannappan, S. J., Burket, J., and Li, W. (2005). Supernovae 2005hh, 2005hi, 2005hj, 2005hk. *IAU Circulars*, 8625.

- Rodríguez, Ó., Clocchiatti, A., and Hamuy, M. (2014). Photospheric Magnitude Diagrams for Type II Supernovae: A Promising Tool to Compute Distances. *The Astronomical Journal*, 148:107.
- Roy, R., Kumar, B., Benetti, S., Pastorello, A., Yuan, F., Brown, P. J., Immler, S., Fatkhullin, T. A., Moskvitin, A. S., Maund, J., Akerlof, C. W., Wheeler, J. C., Sokolov, V. V., Quimby, R. M., Bufano, F., Kumar, B., Misra, K., Pandey, S. B., Elias-Rosa, N., Roming, P. W. A., and Sagar, R. (2011). SN 2008in - Bridging the Gap between Normal and Faint Supernovae of Type IIP. *The Astrophysical Journal*, 736:76.
- Sahu, D. K., Tanaka, M., Anupama, G. C., Kawabata, K. S., Maeda, K., Tominaga, N., Nomoto, K., Mazzali, P. A., and Prabhu, T. P. (2008). The evolution of the peculiar type ia supernova sn 2005hk over 400 days. *The Astrophysical Journal*, 680(1):580–592.
- Silverman, J. M. et al. (2013). Type Ia Supernovae Strongly Interacting with Their Circumstellar Medium. *Astrophys. J. Suppl.*, 207:3.
- Singh, M., Misra, K., Sahu, D. K., Dastidar, R., Gangopadhyay, A., Bose, S., Srivastav, S., Anupama, G. C., Chakradhari, N. K., Kumar, B., Kumar, B., and Pandey, S. B. (2018). Exploring the optical behaviour of a Type Iax supernova SN 2014dt. *Mon. Not. Roy. Astron. Soc.*, 474(2):2551–2563.
- Stritzinger, M. D., Valenti, S., Hoefflich, P., Baron, E., Phillips, M. M., Taddia, F., Foley, R. J., Hsiao, E. Y., Jha, S. W., McCully, C., Pandya, V., Simon, J. D., Benetti, S., Brown, P. J., Burns, C. R., Campillay, A., Contreras, C., Förster, F., Holmbo, S., Marion, G. H., Morrell, N., and Pignata, G. (2015). Comprehensive observations of the bright and energetic type iax sn 2012z: Interpretation as a chandrasekhar mass white dwarf explosion. *Astronomy & Astrophysics*, 573:A2.
- Szalai, T., Zsíros, S., Fox, O. D., Pejcha, O., and Müller, T. (2019). A comprehensive analysis of spitzer supernovae. *The Astrophysical Journal Supplement Series*, 241(2):38.
- Tomasella, L., Cappellaro, E., Benetti, S., Pastorello, A., Hsiao, E. Y., Sand, D. J., Stritzinger, M., Valenti, S., McCully, C., Arcavi, I., Elias-Rosa, N., Harmanen, J., Harutyunyan, A., Hosseinzadeh, G., Howell, D. A., Kankare, E., Morales-Garoffolo, A., Taddia, F., Tartaglia, L., Terreran, G., and Turatto, M. (2016). Optical and near-infrared observations of SN 2014ck: an outlier among the Type Iax supernovae. *Mon. Not. Roy. Astron. Soc.*, 459(1):1018–1038.
- Tully, R. B. and Fisher, J. R. (1977). A new method of determining distances to galaxies. *Astronomy & Astrophysics*, 54:661–673.
- Valenti, S., Fraser, M., Benetti, S., Pignata, G., Sollerman, J., Insnerra, C., Cappellaro, E., Pastorello, A., Smartt, S. J., Ergon, M., Botticella, M. T., Brimacombe, J., Bufano, F., Crockett, M., Eder, I., Fugazza, D., Haislip, J. B., Hamuy, M., Harutyunyan, A., Ivarsen, K. M., Kankare, E., Kotak, R., Lacluyze, A. P., Magill, L., Mattila, S., Maza, J., Mazzali, P. A., Reichart, D. E., Taubenberger, S., Turatto, M., and Zampieri, L. (2011). SN 2009jf: a slow-evolving stripped-envelope core-collapse supernova. *Mon. Not. Roy. Astron. Soc.*, 416(4):3138–3159.
- Yamanaka, M., Maeda, K., Kawabata, K. S., Tanaka, M., Tominaga, N., Akitaya, H., Nagayama, T., Kuroda, D., Takahashi, J., Saito, Y., Yanagisawa, K., Fukui, A., Miyanoshita, R., Watanabe, M., Arai, A., Isogai, M., Hattori, T., Hanayama, H., Itoh, R., Ui, T., Takaki, K., Ueno, I., Yoshida, M., Ali, G. B., Essam, A., Ozaki, A., Nakao, H., Hamamoto, K., Nogami, D., Morokuma, T., Oasa, Y., Izumiura, H., and Sekiguchi, K. (2015). Oister optical and near-infrared observations of type iax supernova 2012z. *The Astrophysical Journal*, 806(2):191.

A Decline Rates

Table A.1: Absolute magnitude decline rates for each filters

Object	Epoch (days)	B	g	V	r	i
		(mag.day ⁻¹)				
SN 2014dt	250-350	0.013	0.011	0.011	0.004	0.003
	500-600	0.008	0.011	0.011	0.02	0.017
	700-800	-	-	-	-	-
SN 2005hk	250-350	0.015	0.015	0.018	0.013	0.009
	500-600	0.015	0.015	0.018	0.012	0.018
SN 2012Z	250-350	0.011	0.012	0.02	0.019	0.019
	500-600	0.004	0.012	0.009	0.007	0.012
Object	Epoch (days)	J	H	K	S36	S45
		(mag.day ⁻¹)				
SN 2014dt	250-350	0.004	0.0012	-0.003	-0.001	0.011
	500-600	0.02	0.019	0.0044	-0.0019	-0.0015
	700-800	-	-	-	0.014	0.0083
SN 2005hk	250-350	0.007	0.013	-	-	-
	500-600	0.007	0.013	-	-	-
SN 2012Z	250-350	0.008	0.009	-	-	-
	500-600	0.008	0.005	-	-	-

Table A.2: Bolometric luminosity decline rates (log(erg.s⁻¹).day⁻¹)

Object	Filter range	Epoch (days)		
		25-75	250-300	850-900
SN 2014dt	All Filters	0.0087	0.0016	0.0031
	Optical + N-IR	0.0088	0.0017	0.0047
	Optical	0.014	0.0025	0.0045
	Two-Component Model	0.013	0.0054	0.0040
SN 2005hk	Optical + N-IR	0.014	0.0043	-
SN 2012Z	Optical + N-IR	0.014	0.0062	0.0019